Electrochemical Properties and Local Structure of the TEMPO/TEMPO$^+$ Redox Pair in Ionic Liquids

Kateryna Goloviznina[†] and Mathieu Salanne[*,†]

†*Sorbonne Université, CNRS, Physicochimie des Électrolytes et Nanosystèmes Interfaciaux, F-75005 Paris, France*

‡*Réseau sur le Stockage Electrochimique de l'Energie (RS2E), FR CNRS 3459, 80039 Amiens Cedex, France*

¶*Institut Universitaire de France (IUF), 75231 Paris, France*

E-mail: mathieu.salanne@sorbonne-universite.fr

Abstract

Redox-active organic species play an important role in catalysis, energy storage, and biotechnology. One of the representatives is 2,2,6,6-tetramethylpiperidine-1-oxyl (TEMPO) radical, used as a mediator in organic synthesis and considered a safe alternative to heavy metals. In order to develop a TEMPO-based system with well-controlled electrochemical and catalytic properties, a reaction medium should be carefully chosen. Being highly conductive, stable, and low flammable fluids, ionic liquids (ILs) seem to be promising solvents with easily adjustable physical and solvation properties. In this work, we give an insight into the local structure of ILs around TEMPO and its oxidized form, TEMPO$^+$, underlining striking differences in solvation of these two species. The analysis is coupled with a study of thermodynamics and kinetics of oxidation in the frame of Marcus theory. Our systematic investigation includes imidazolium, pyrrolydinium, and phosphonium families combined with anions of different size, polarity, and flexibility, opting to provide a clear and comprehensive picture of the impact of the nature of IL ions on the behavior of radical/cation redox pair. The obtained results will help to explain experimentally observed effects and to rationalize the design of TEMPO/IL systems.

Introduction

2,2,6,6-Tetramethylpiperidine-1-oxyl (TEMPO, Fig. 1) is primarily known as a stable, sustainable, and metal-free mediator for a wide range of redox reactions, including oxidation of alcohols, amines, alkenes, etc.[1–3] It is typically used in its oxidized form, $TEMPO^+$, easily generated electrochemically,[4] and the midpoint potential of the $TEMPO/TEMPO^+$ couple reaches 0.73–0.77 eV (*vs* NHE) in water.[2]

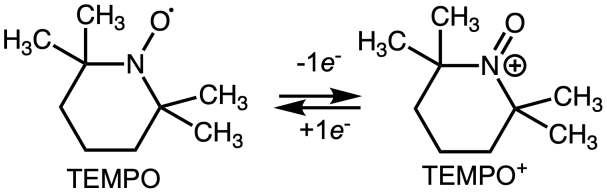

Figure 1: TEMPO redox reaction.

Application of TEMPO and its derivatives often goes beyond simple redox reactions. It is used in energy storage devices (dye-sensitized solar cell, redox flow batteries, $Li-O_2$ batteries, supercapacitors, etc.),[5–8] as spin labels in electron spin resonance (ESR) technique,[9,10] as catalyst for biomass and cellulose processing[11,12] and for the oxydation of alcohols to aldehydes.[13] Therefore, finding a way of tuning the reactivity of TEMPO becomes an important issue in the context of the development of new TEMPO-based systems and improvement of the performance of the existing ones.

One of the ways to control the electrochemical properties of TEMPO is to use solvents with adjustable properties. Here, ionic liquids (ILs) serve as promising candidates. Among the advantages of ILs, one should mention high conductivity, large electrochemical window, good thermal stability, low flammability, and negligible vapor pressure. Thanks to a tight balance between diverse intermolecular forces, ionic fluids are capable to dissolve a broad variety of solutes. Their properties can be modified by choosing a suitable combination of ionic head groups and side chains.[14–16]

Some systematic studies of the effect of the nature of IL ions on the redox properties of TEMPO are already present in the literature. Delorme *et al.*[4] investigated efficiency, selectivity and reaction kinetics of alcohol oxidation with TEMPO as a function of IL solvent composition. They demonstrated better performance of NTf_2-based ILs than common molecular solvents, underlining their selectivity towards primary alcohols. A correlation between the basicity of an anion and the redox potential of TEMPO was revealed. In addition, Minteer *et al.*[17] pointed out that some ILs can prevent TEMPO from degradation during alcohol oxidation in a basic medium. A combined experimental and theoretical work by Wylie *et al.*[18–21] was focused on the use of TEMPO/IL systems in redox flow batteries. It was shown that depending on the nature of IL ions, different stabilization is observed for the radical and its oxidized form, which allows controlling the redox potential of TEMPO by target modifications of the IL structure.

The observed effects clearly arise from the specific interaction of the radical and its oxidized form with a solvent. While interactions of TEMPO with IL ions were investigated in a QM study by Liu and co-workers[22] and by ESR measurements of Strehmel *et al.*,[23,24] data on those of the $TEMPO^+$ cation are rather scarce. Indeed, almost no information on changes in the local structure of TEMPO upon oxidation is available in the literature.

In the present work, we aim to provide a complete description of the influence of IL nature on the microenvironment of TEMPO and $TEMPO^+$ for main IL families. We will establish structure-property relationships that allow forecasting electrochemical behavior of the nitroxide radical in different ionic fluids. As a method, we chose polarizable molecular dynamics simulations, a state-of-art tool in the modeling of ionic liquids,[25] which guarantees a correct prediction of structural and dynamic properties of the systems of interest. A classical Marcus theory,[26,27] which is a simple but powerful approach, will be used to estimate redox properties of TEMPO/TEMPO$^+$ couple, giving an insight into the kinetics of the electron transfer process.

Methodology

Simulation details

Molecular dynamics simulations of periodic cubic boxes were performed in OpenMM[28] software. The boxes contained 1 solute molecule surrounded by 300 ion pairs of ionic liquid, prepared using PACKMOL[29] and fftool[30] utilities. An extra anion was added to the systems containing a TEMPO$^+$ cation to zero the total charge of the box during the structural analysis, while an equal number of IL ions was retained for free energy calculations. We chose imidazolium ($\mathrm{C_nC_1im^+}$, $n = 2, 4, 8$), pyrrolidinium($\mathrm{C_nC_1pyrr^+}$, $n = 4$) and phosphonium ($\mathrm{P^+_{nnn1}}$, $n = 4$) families of ionic liquid cations with various side chain length (from ethyl to octyl) and combined them with tetrafluoroborate ($\mathrm{BF_4^-}$), dicyanimide ($\mathrm{DCA^-}$), methanesulfonate (or mesylate, $\mathrm{MsO^-}$), and bis(trifluoromethane)sulfonimide (or bistriflimide, $\mathrm{NTf_2^-}$) anions. The structural formulae of ions are shown in Fig. 2. In total, 8 different ionic liquids were considered as solvents.

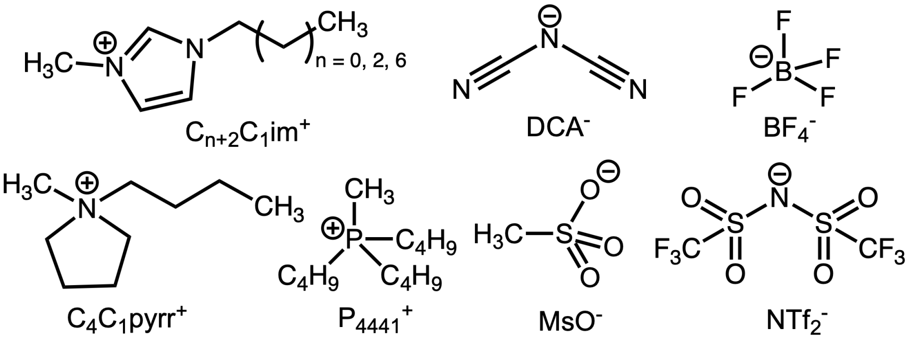

Figure 2: Structural formulae of ILs ions.

Each simulation consisted of 5 ns equilibration in the NPT ensemble followed by a 100 ns production run in the NVT ensemble. The time step was set to 1 fs. A cut-off of 12 Å was used for non-bonded interactions, and a tail correction was applied for energy and pressure. Long-range electrostatic interactions were computed using Particle Mesh Ewald (PME) method with the tolerance of 10^{-5}. Bonds involving hydrogen atoms were constrained using the SHAKE algorithm. Dual Langevin thermostat and Monte Carlo barostat were used for temperature and pressure control. The temperature and the pressure were set to 298 K and 1 bar, respectively.

Explicit polarizable effects were represented by Drude induced dipoles.[31] Each Drude dipole consisted of a positively charged Drude core (DC) and a negatively charged Drude particle (DP, $m_{\mathrm{DP}} = 0.4\,\mathrm{a\,u}$), attached to the core by a harmonic spring ($k_{\mathrm{DC-DP}} = 4184\,\mathrm{kJ\,mol^{-1}}$). Drude charges were evaluated from atomic polarizabilities, $q_{\mathrm{DP}} = -\sqrt{\alpha k_{\mathrm{DC-DP}}}$. Only heavy atoms were considered as polarizable. In order to approximate the self-consistent regime, the Drude degrees of freedom were kept at 1 K. Thole damping function[32,33] with the universal parameter $a = 2.6$ was used to smear short-range interactions between the induced dipoles and was combined with a hard wall constraint[34] with the maximum $\mathrm{DC} - \mathrm{DP}$ distance of 0.2 Å to ensure the stability of the trajectories. The CL&Pol polarizable force field[35–37] was used for simulating ionic liquids, and TEMPO was modeled by means of the previously developed polarizable model,[38] with the adjusted non-bonded interaction parameters (a complete description given in SI).

Structure analysis of the equilibrium trajectories was performed in TRAVIS,[39,40] while VMD[41] was used for the visualization.

Free energy calculations

Any electrochemical process can be written in terms of the redox half-reactions,

$$\mathrm{Red} \leftrightarrows \mathrm{Ox} + e^{-},$$

where Red refers to reduced (denoted further as 0) and Ox to oxidized (denoted as 1) states. Such reactions are generally studied by molecular dynamics using the energy difference between these two states for a given solvent configuration $\mathbf{R}_N$, which is called the vertical energy gap (VEG) $\Delta E(\{\mathbf{R}_N\})$,

$$\Delta E(\{\mathbf{R}_N\}) = E_1(\{\mathbf{R}_N\}) - E_0(\{\mathbf{R}_N\}), \tag{1}$$

as a reaction coordinate.[42] According to Marcus theory,[26,27] the probability of observing a given ΔE value obeys a Gaussian distribution,

$$P_i(\Delta E) = \sqrt{\frac{1}{4\pi k_\mathrm{B} T \lambda_i}} \exp\left(- \frac{(\Delta E - \langle \Delta E \rangle_i)^2}{4 k_\mathrm{B} T \lambda_i} \right), \tag{2}$$

where λ_i is a reorganization energy and $\langle \Delta E \rangle_i$ is a mean VEG of a state i. From the corresponding probabilities, Landau free energies can be evaluated as

$$A_i(\Delta E) = -k_\mathrm{B} T \log(P_i(\Delta E)) + \bar{A}_i. \tag{3}$$

where $\bar{A}_i$ is mean free energy of a state i.

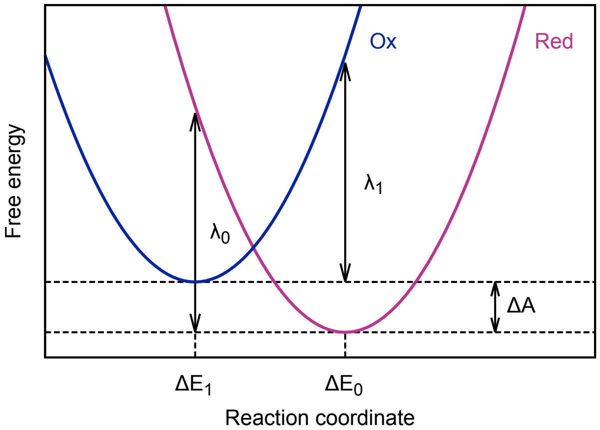

Figure 3: Marcus diabatic free energy profiles

Typical diabatic free energy curves are shown in Fig 3, being characterized by the reaction free energy ΔA and the reorganization energy λ. The reaction free energy corresponds to a vertical difference between two minima, also evaluated from the mean VEGs values,

$$\Delta A = \frac{1}{2}\Big(\langle \Delta E_0 \rangle + \langle \Delta E_1 \rangle\Big). \tag{4}$$

The reorganization energy is the energy needed to switch the equilibrium geometry of one state to the equilibrium geometry of another while staying on the free energy curve of the first state. It is related to the curvature of the diabatic free energy curves, described by parabolas,[26,27]

$$A_i(\Delta E) = A_{\min,i} + \frac{1}{4\lambda_i}\Big(\Delta E - \langle \Delta E \rangle_i\Big), \tag{5}$$

Here, individual curvatures are equal, $\lambda_0 = \lambda_1 = \lambda$, and the reorganization energy can be expressed through the VEGs,

$$\lambda = \frac{1}{2}\Big(\langle \Delta E_0 \rangle - \langle \Delta E_1 \rangle\Big). \tag{6}$$

The parabolas are in relation to each other, and the free energy difference between the oxidized and the reduced states for a given configuration corresponds to VEG,

$$A_1(\Delta E) - A_0(\Delta E) = \Delta E. \tag{7}$$

From the kinetic point of view, another important characteristic is a free energy barrier, measured as a difference between the free energy in the cross point of two states and the free energy minimum of the initial state. It depends both on the reaction free energy and reorganization energy,

$$\Delta A' = \frac{(\lambda + \Delta A)^2}{4\lambda} \tag{8}$$

Then, from the free energy barrier, the reaction rate constant can be then estimated through Arrhenius equation,

$$k = \mathcal{A} \exp\left(- \frac{\Delta A'}{k_\mathrm{B} T} \right), \tag{9}$$

where T is the temperature, k_B is the Boltzmann constant, and $\mathcal{A}$ is an exponential prefactor. For diabatic free energy curves, the prefactor is typically calculated through Fermi golden rule.[43] Here we hypothesize that for a given redox species it is system-independent so that the relative rate constants in different solvents can be easily compared.

Following the main statements of Marcus theory, we then calculated free energies and reaction rates of TEMPO oxidation in different ionic liquids by a two-step approach. First, the non-bonded (both intra- and intermolecular) interactions of TEMPO were modified from the initial state (radical, 0) to the final (cation, 1), while keeping the bonded interactions unchanged, and the free energies were evaluated through eq. 4.

This step also included an extra check of a linear response theory since deviations from Marcus theory are often reported in the literature.[44–46] For that, a few additional systems with a mixed Hamiltonian were simulated. The mixed Hamiltonian was defined as

$$\begin{aligned} E_\eta(\{\mathbf{R}_N\}) &= (1-\eta)E_0(\{\mathbf{R}_N\}) + \eta E_1(\{\mathbf{R}_N\}) \\ &= E_0(\{\mathbf{R}_N\}) + \eta \Delta E(\{\mathbf{R}_N\}) \end{aligned} \tag{10}$$

where η is a coupling parameter varying from 0 (radical) to 1 (cation) with a step of $d\eta = 0.25$. Thermodynamic integration was then used to compute the free energies,

$$\Delta A = \int_0^1 d\eta \left\langle \frac{dE_\eta(\{\mathbf{R}_N\})}{d\eta} \right\rangle = \int_0^1 d\eta \langle \Delta E(\{\mathbf{R}_N\}) \rangle_\eta, \tag{11}$$

and the resulting values were compared to those obtained *via* eq. 4

During the second step, in the system with already modified non-bonded interactions, the bonded part was switched from that of the radical (R) to that of the cation (C) at once. Free energies were assessed by means of Bennett Acceptance Ratio (BAR),[47] applied to the corresponding energy distributions,

$$\frac{Q_{\mathrm{R}}}{Q_{\mathrm{C}}}=\frac{\langle\{1+\exp[\beta(E_{\mathrm{R}}-E_{\mathrm{C}}+C)]\}^{-1}\rangle}{\langle\{1+\exp[\beta(E_{\mathrm{C}}-E_{\mathrm{R}}-C)]\}^{-1}\rangle}\exp(\beta C), \tag{12}$$

where Q_{R} and Q_{C} are partition function of states R and C, $\beta = 1/(k_{\mathrm{B}}T)$, and $C = \ln[(Q_{\mathrm{R}}n_{\mathrm{C}})/(Q_{\mathrm{C}}n_{\mathrm{R}})]$ is a constant iteratively evaluated though a self-consistent procedure.

This gave rise to 0R, 0.25R, 0.50R, 0.75R, 1R, and 1C equilibrium trajectories, with the number corresponding to the non-bonded potential parameters and the letter to the bonded ones. An extra 0C system was considered for $[C_2C_1\mathrm{im}][\mathrm{NTf}_2]$ to check the independence of free energy from a calculation path (discussed in SI). For each trajectory, one or several VEGs were computed in order to reach the free energies.

Results and discussion

Local structure analysis

We first focus on the differences in local environments of the TEMPO radical and the TEMPO^{+} cation. As was mentioned above, the state in which all interaction parameters correspond to the TEMPO radical is denoted as 0R and the one with those of the TEMPO^{+} cation as 1C. In order to present some general trends, we have chosen $[C_2C_1\mathrm{im}][\mathrm{NTf}_2]$ as an example of the solvent.

The TEMPO radical mainly acts as a hydrogen-bond acceptor, interacting with the $C_2C_1\mathrm{im}^{+}$ cation. It forms weak H-bonds with hydrogen atoms of the imidazolium ring (H_{CR} and H_{CW}) through its nitroxide group at a distance of 2.50 Å, as shown in Fig. 4a. The $\mathrm{C{-}H\cdots O_T}$ angles are greater for H_{CW} atoms than for H_{CR} (Fig. 5a-b), being in the range of 110–180° and 100–160°, respectively. The first coordination shell is formed at a distance of 3.97 Å and includes 0.37 H_{CR} and 0.77 H_{CW} atoms. A weaker interaction is observed with hydrogen atoms of N-methyl group and N-methylene groups of the cation: The peaks are

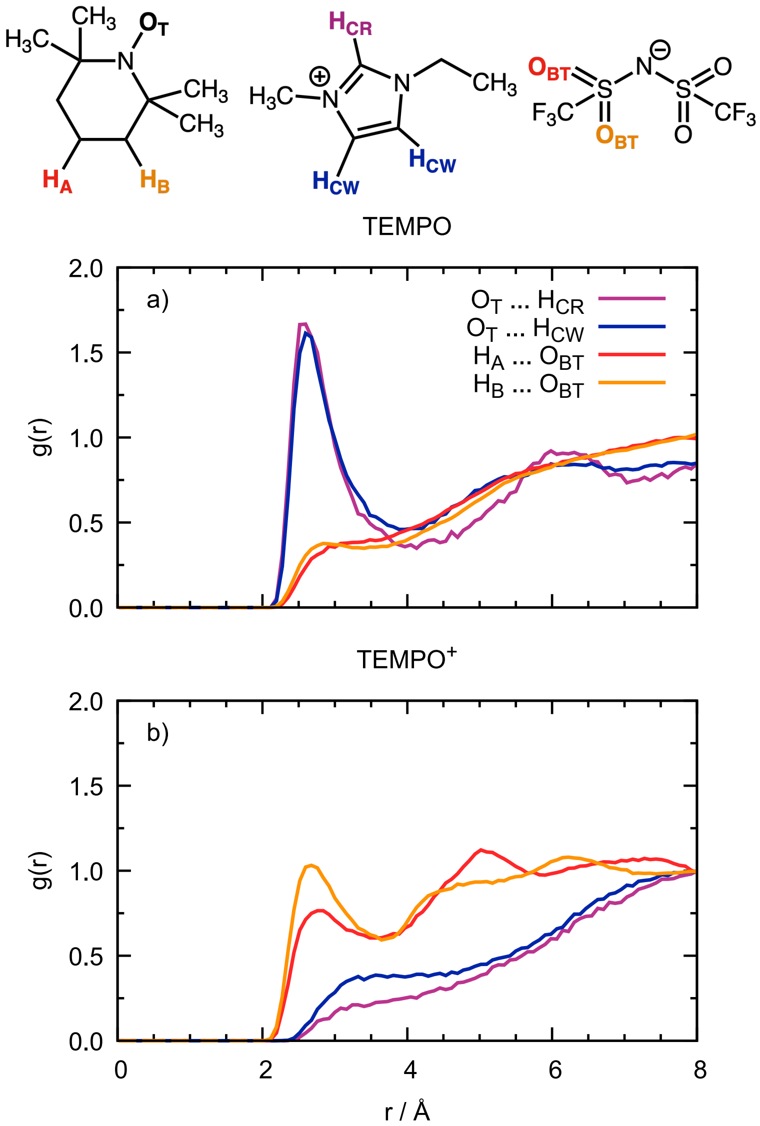

Figure 4: Radial distribution functions of atoms of $[C_2C_1im][NTf_2]$ IL around (a) TEMPO and (b) $TEMPO^+$. Atomic labels are given in bold with matching colors in the corresponding scheme.

shifted to 2.68 Å, the intensities are lower by about 30 % (Fig. S3a) and the angles decrease to 100–140° for the N-methylene group and to 90–130° for the N-methyl group (Fig. S4a-b). No specific interaction between TEMPO and the anion is observed (Fig. 4a).

The formation of such H-bonds agrees well with a recent *ab initio* study by Liu *et al.*[22] They proposed the interaction of TEMPO radical with the H_{CR} atom of the $C_1C_1im^+$ cation to be the dominant one. The QM geometry optimization of a single pair in a gas phase gave

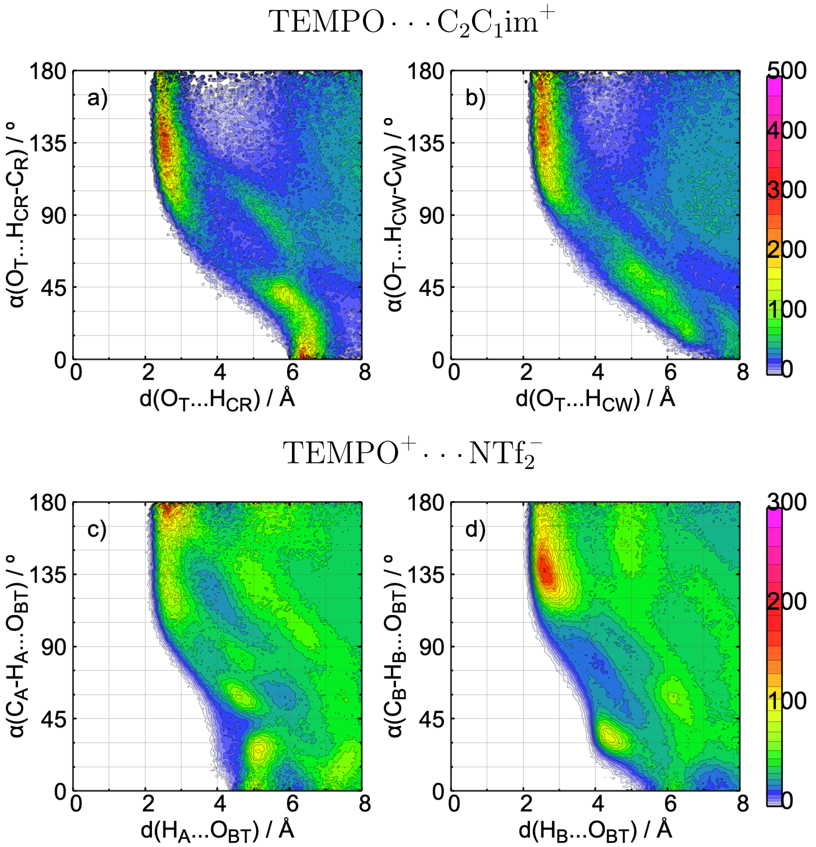

TEMPO $\cdots$ $C_2C_1im^+$

TEMPO$^+$ $\cdots$ NTf_2^-

Figure 5: Probability contours revealing hydrogen bonds of TEMPO/TEMPO$^+$ with $[C_2C_1im][NTf_2]$. The x-axes represent the distances between the H atoms and the acceptor atoms (A). The y-axis represents the angles formed by the D−H $\cdots$ A hydrogen bonds, where D is a donor atom attached to the hydrogen. The labels are given in Fig. 4; C_R, C_W, C_A and C_B are carbon atoms bonded to H_{CR}, H_{CW}, H_A and H_B atoms, respectively.

a shorter H-bond than we observe in MD, with a distance of 1.95 Å and an angle of 144°. The TEMPO $\cdots$ $C_1C_1im^+$ complex is stabilized by side N-methyl groups interacting with the nitroxide group.

The same group of authors revealed a π-radical complex between the imidazolium ring and the nitroxide group. The characteristic distance between the nitrogen atoms of $C_1C_1im^+$ and TEMPO was about 2.7 Å, with the radical being almost perpendicular to the ring plane. From the energetic point of view, this complex was less stable than the H-bonded complex.

In MD simulations, this interaction is observed at longer distances (Fig. 6). The RDF of O_T atoms around the center of the ring (CoR) of imidazolium shows a prominent wide peak

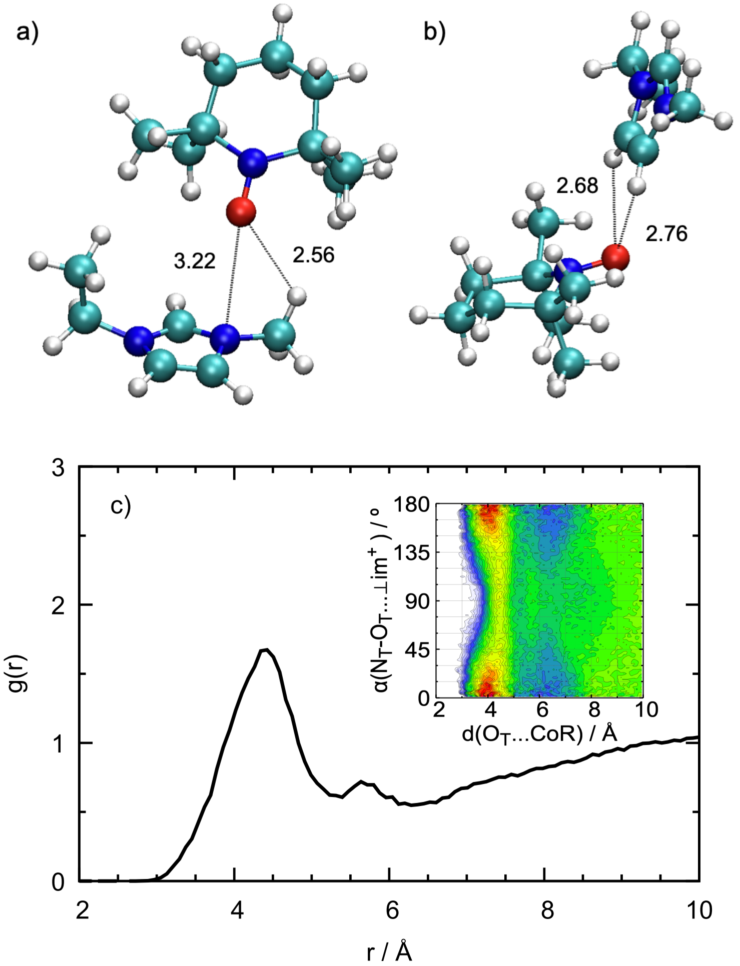

Figure 6: Snapshots of $C_2C_1im^+ \cdots$TEMPO π-radical complex (a) and H-bonding between the nitroxide group of TEMPO and hydrogen atoms of imidazolium ring (b).The distance between the oxygen atom of TEMPO and the nitrogen atom of the imidazolium ring equals 3.2 Å (a) and 4.6 Å (b, not shown). Note, that in both cases the $O_T{-}N_T$ vector is almost perpendicular to the plane of the ring of the cation. (c) Radial distribution function of O_T atoms of the TEMPO radical around the centre of the ring (CoR) of $C_2C_1im^+$ in $[C_2C_1im][NTf_2]$. Inset : The probability contour revealing the orientation of TEMPO with respect to the imidazolium plane. The x-axis represents the distances between the O_T atoms and CoR. The y-axes represent the angles formed by the $O_T{-}N_T$ vector and the normal vector to the imidazolium plane.

with a maximum at 4.36 Å. The $O_T{-}N_T$ vector and the normal vector to the imidazolium plane are found in parallel or antiparallel orientation, meaning that TEMPO is perpendicular to the aromatic ring. The asymmetricity of the RDF peak points at the presence of several contributions arising from different configurations. Indeed, according to Fig. 6a, at shorter distances the radical is placed above the imidazolium plane, forming the π-radical complex, which is supported by a weak H-bond with N-methyl (or N-methylene) group of the $C_2C_1im^+$ cation. At longer separations, TEMPO sits on the side, participating in a direct H-bond with hydrogen atoms of the imidazolium ring, as illustrated by Fig. 6b. Both for H-bonded and for π-radical complexes, the intramolecular distances are shorter in the QM study[22] than we observed in MD simulations. This can be explained by the absence of a solvation environment during *ab initio* geometry optimizations, which resulted in enhanced interactions between TEMPO radical and $C_1C_1im^+$ cation.

On the contrary, the $TEMPO^+$ cation acts as a hydrogen-bond donor, forming doubly ionic H-bonds[48] with the NTf_2^- anion. The $C_2C_1im^+$ cation, is then pushed away from the positively charged $TEMPO^+$. Weak H-bonds are formed between oxygen atoms of bistriflimide and H_A and H_B atoms of $TEMPO^+$, with $H \cdots O_{BT}$ distance of 2.65 Å (Fig. 4b). The normalized intensity of the $H_B \cdots O_{BT}$ peak is greater than that of $H_A \cdots O_{BT}$, pointing at more probable interaction with these H_B methylene groups. This is also reflected in a greater coordination number of H_B atoms than that of H_A (1.02 *vs* 0.84, respectively) in the first coordination shell, formed at 3.55 Å. The observed effects can be explained by a higher partial charge at H_B atom comparing to H_A (Table S1). Surprisingly, the H_A atoms form completely linear H-bonds (Fig. 5c), with a narrow angle distribution, of about 165–180°, while for the H_B atoms, H-bonds are bent to 120–145° (Fig. 5d). The latter results from spacial proximity of several methyl groups in $TEMPO^+$ that leads to a steric hindrance around H_B atoms and hampers approaching of a bulky NTf_2^- to them. The hydrogen atoms of those methyl groups (denoted as H_D in SI) weakly interact with the anion, even despite the close presence of the positively charged $N^+{=}O$ moiety. A peak with an intensity close to 1 times relative density appears at 2.72 Å (Fig. S3b, S4c).

Let's now investigate the effect of the IL nature on the local structure of TEMPO and $TEMPO^+$. Since TEMPO mainly interacts with the cation, we will study the influence of the side chain length by using $C_2C_1im^+$, $C_4C_1im^+$, and $C_8C_1im^+$ cations, and the nature of the cation by comparing $C_4C_1im^+$, $C_4C_1pyrr^+$ and P_{4441}^+ system. In all cases, NTf_2^- will be taken as an anion. Since $TEMPO^+$ prefers interaction with the anions, we considered the anions with a different size, flexibility and H-bond basicity, namely BF_4^-, DCA^-, MsO^-, and NTf_2^-, combined with the $C_2C_1im^+$ cation.

As discussed before, hydrogen bonding occurs between O_T atom of TEMPO and hydrogen atoms of the cation. In order to simplify the analysis, we will focus only on H_{CR} atoms of imidazolium cations, and H_{1A} atoms of all N-methylene and P-methylene groups of pyrrolidinium and phosphonium cations. These hydrogen atoms demonstrate the highest RDF peaks in each case (Fig. S5) and are known to have enhanced acidity and reactivity.[49–52]

In the series of imidazolium cations with different side chain lengths, the intensity of the first RDF peak at about 2.50 Å is the greatest for $C_8C_1im^+$, while for $C_2C_1im^+$ and $C_4C_1im^+$ the probabilities are close (Fig. 7a). This is the classical example of the dilution effect, according to which the systems with a greater number of atoms of all kinds show higher RDF peaks. Indeed, the coordination number of the first coordination shell ($r_{min} = 4.01$ Å) equal 0.38 for $C_2C_1im^+$, being only $0.28 - 0.29$ for $C_4C_1im^+$ and $C_8C_1im^+$ cations (Table S4). The increase of the side chain length does not affect the geometry of this H-bonds, according to Fig. 5a and 8a-b.

In the series of the cations with different head groups, it becomes even more problematic to compare the intensities of the RDF peaks (Fig. 7a). We consider one H_{CR} atom for $C_4C_1im^+$ and six H_{1A} atoms for $C_4C_1pyrr^+$ and P_{4441}^+ cations. The coordination numbers are 1.57 for $C_4C_1pyrr^+$ and 1.35 for P_{4441}^+ at a distance of 3.82 Å, which can be divided by six to be compared to 0.28 atoms of $C_4C_1im^+$. As a result, in all systems, the coordination number equals about $0.25 - 0.28$ per one hydrogen atom. Obviously, the nature of the cation head group should affect the geometry of the corresponding H-bond. The maximum probability of $O_T \cdots H$ distance is shifted to 2.60 Å in $C_4C_1pyrr^+$ and P_{4441}^+ ILs, and the $O_T \cdots H{-}C$ angle increases in the row $C_4C_1im^+ < C_4C_1pyrr^+ < P_{4441}^+$ (Fig. 8a,c-d).

The interaction of $TEMPO^+$ with different anions will be discussed considering the H_B

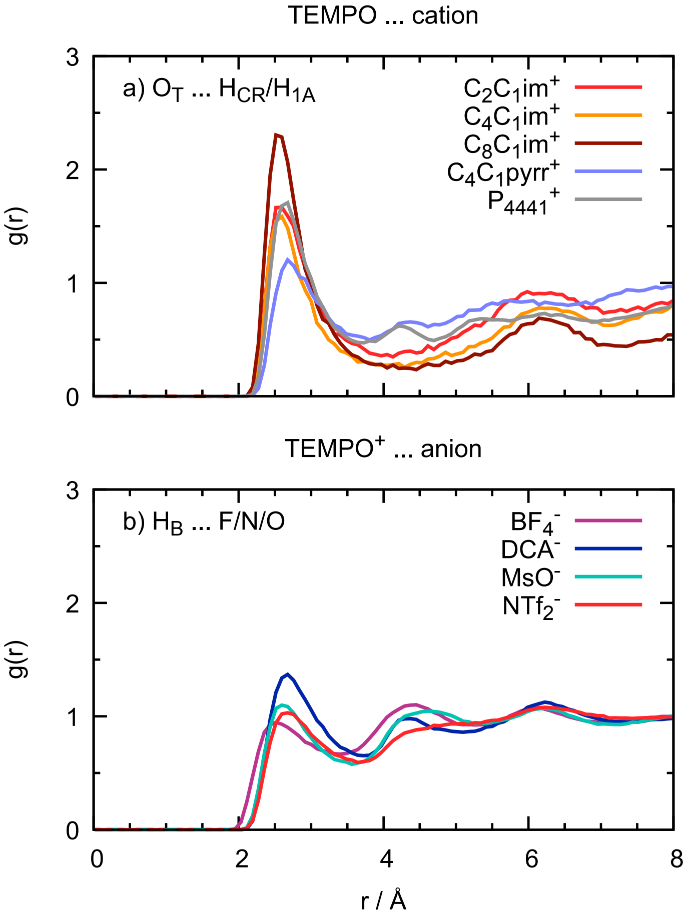

Figure 7: Radial distribution functions of IL atoms around (a) TEMPO and (b) TEMPO^+. The top plot corresponds to the interaction of $\mathrm{O_T}$ atom of TEMPO with $\mathrm{H_{CR}}$ atom of imidazolium cations or with $\mathrm{H_{1A}}$ atoms of N-methylene group of pyrrolidinium or P-methylene group of phosphonium cation in the series of $\mathrm{NTf_2}$-based ILs. The bottom plot corresponds to the interaction of $\mathrm{H_B}$ atom of TEMPO^+ with oxygen atoms of mesylate or bistriflimide, terminal nitrogen atoms of dycyanimide, fluorine atoms of tetrafluoroborate in the series of $\mathrm{C_2C_1}$im-based ILs.

atom as an example. As acceptor atoms, we chose oxygen atoms of $\mathrm{NTf_2^-}$ and $\mathrm{MsO^-}$, terminal nitrogen atoms of $\mathrm{DCA^-}$. In the case of $\mathrm{BF_4^-}$ anion, we cannot truly talk about H-bonding with fluorine atoms, but we will use this atom type for RDFs and probability contour plots for simplicity of representation at once with other systems.

In the series of the anions, the $\mathrm{H_B}\cdots\mathrm{F/N/O}$ distance correlates with a size of the corresponding acceptor atom, ranging from 2.48 Å for $\mathrm{BF_4^-}$ to 2.65 Å for $\mathrm{NTf_2^-}$. Peak intensities of all interactions are similar (Fig. 7b) and are normalized both by a different number of ac-

TEMPO···cation

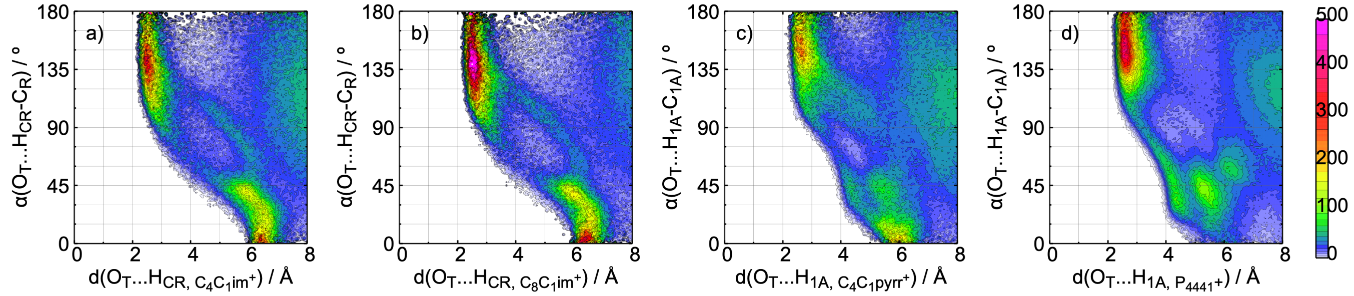

TEMPO$^+$···anion

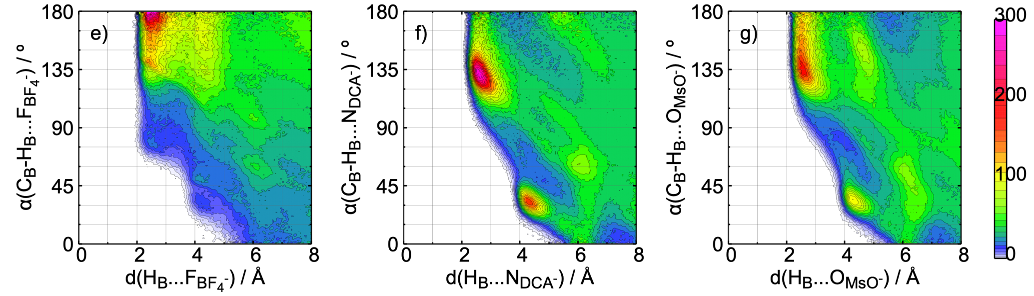

Figure 8: Probability contours revealing interactions of TEMPO/TEMPO$^+$ with ILs. The labels of hydrogen atoms are explained in the text; C_R, C_1A and C_B are carbon atoms bonded to H_{CR}, H_{CW}, H_{1A} and H_B atoms, respectively.

ceptor atoms per anion and by a different total number of atoms in the system. The position of the first coordination shell varies from 3.22 Å to 3.75 Å depending on the anion type (see Table S4 for the details). The CN increases in the row $NTf_2^- < MsO^- < DCA^- < BF_4^-$ that barely correlates to the basicity of the anions.[53] By normalising these values by the number of acceptor atoms per ion, we obtain a completely different picture, $BF_4^- < NTf_2^- < MsO^- < DCA^-$, in which more basic MsO$^-$, DCA$^-$ anions are found more often near TEMPO$^+$ cation. The geometry of this interaction is quite different for all the systems. For the BF_4^- anion, the $C_B{-}H_B\cdots F$ angle is about 170–180° (Fig. 8e), meaning that the hydrogen atom align with the B−F vector and is not situated in a hollow formed by three neighboring fluorine atoms. Smaller, but well localized angles are observed for the DCA$^-$ anion (Fig. 8f), with the average value close to 130°. The geometry of interaction of MsO$^-$ (Fig. 8g) with TEMPO$^+$ is very close to that of NTf_2^- (Fig. 5d), though the angle distribution for MsO$^-$ is wider, comprising greater angles.

When increasing the length of a carbon side chain of a cation, non-polar dispersive interactions with methyl groups of TEMPO radical may occur. The experimental data on this subject are contesting. Compton *et al.*[54] made an assumption of preferable solvation of TEMPO by non-polar domains of ionic fluids based on their results on the rotation dynamics of the radical in [$P_{14.666}$][NTf_2]. On the contrary, using ESR spectroscopy Strehmel[23] showed that TEMPO cannot detect micropolarity changes of imidazolium-based ILs with side chain length up to $n = 10$.

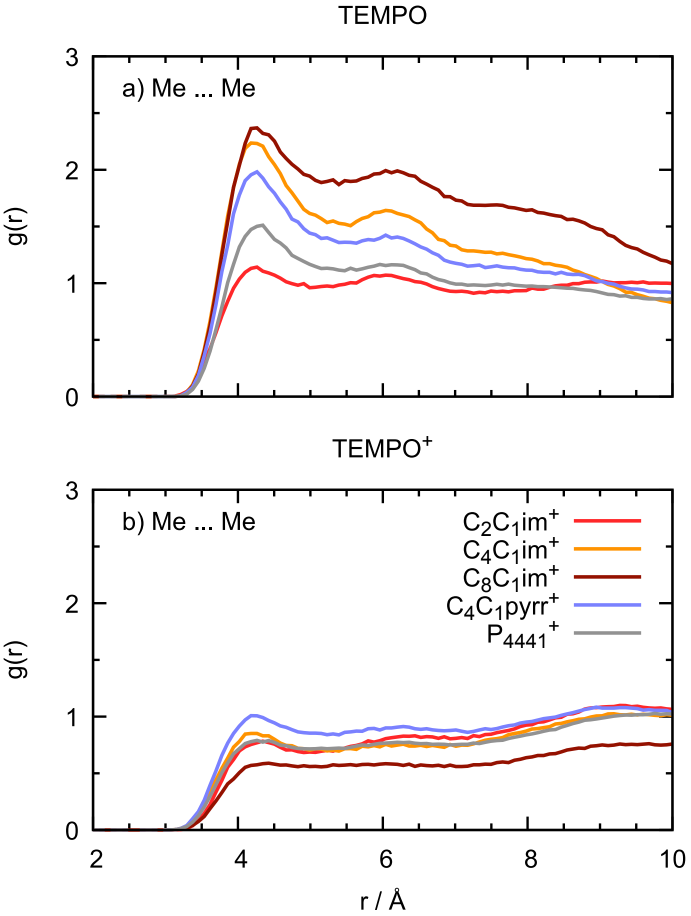

Figure 9: Radial distribution functions of carbon atoms of terminal methyl groups of NTf_2-based ILs around carbon atoms of methyl groups (a) TEMPO and (b) $TEMPO^+$.

In our study, we observe some dispersive interaction of TEMPO already visible with $C_4C_1im^+$, and $C_8C_1im^+$ cations, in which a RDF peak between carbon atoms of the terminal methyl group and the methyl groups of TEMPO appears at about 4.20 Å (Fig. 9a). Nevertheless, comparing intensities is not straightforward due to the dilution effect. The coordination number at the first minimum ($r_{min} = 5.20$ Å) is bigger for $C_4C_1im^+$ than for $C_8C_1im^+$, being equal to 1.49 and 1.31, respectively. A similar trend is observed for $C_4C_1pyrr^+$ and P_{4441}^+ cations, with corresponding coordination numbers of 1.24 and 2.17. Here, three terminal carbon atoms are considered for P_{4441}^+. Therefore, we confirmed the hypothesis of the presence of long alkyl side chain of cations near TEMPO, however in our systems TEMPO is not fully solvated by lipophilic regions. This dispersive interaction diminishes upon oxidation, as can be seen in Fig. 9b, leading to a conclusion that the whole cation (and not only its head group) is repelled from $TEMPO^+$.

Therefore, in all the cases, TEMPO prefers the interaction with the IL cation, while the IL anion is found nearby oxidized $TEMPO^+$ species. This indicates a different solvation environment of these two redox forms, that might be reflected in their electrochemical properties.

Free energy calculations

Let us consider 0R as an initial state with both non-bonded and bonded interactions parameters of the TEMPO radical, and 1C as a final state with the parameters of the $TEMPO^+$ cation. Similarly to the previous subsection, we chose $[C_2C_1im][NTf_2]$ solvent as an example. Normalized probability distributions of VEG, computed for $(0R \rightarrow 1C)_{0R}$ and $(0R \rightarrow 1C)_{1C}$ processes, with the subscript denoting the configurations space, are presented in Fig. 10a. Both distributions can be approximated with Gaussians, but the intensity and standard deviations of each individual fit (values given in Table S5) are rather different, pointing at a violation of Marcus theory.

In order to obtain a more detailed description of the electron transfer process and to disclose the reasons of non-linearity, we split the reaction path into a few consecutive steps, namely, $0R \rightarrow [0.25R \dashrightarrow 0.50R \dashrightarrow 0.75R] \rightarrow 1R$ and $1R \rightarrow 1C$. During the first step, the non-bonded interactions (Lennard-Jones, Couloumb, and polarization terms) are either

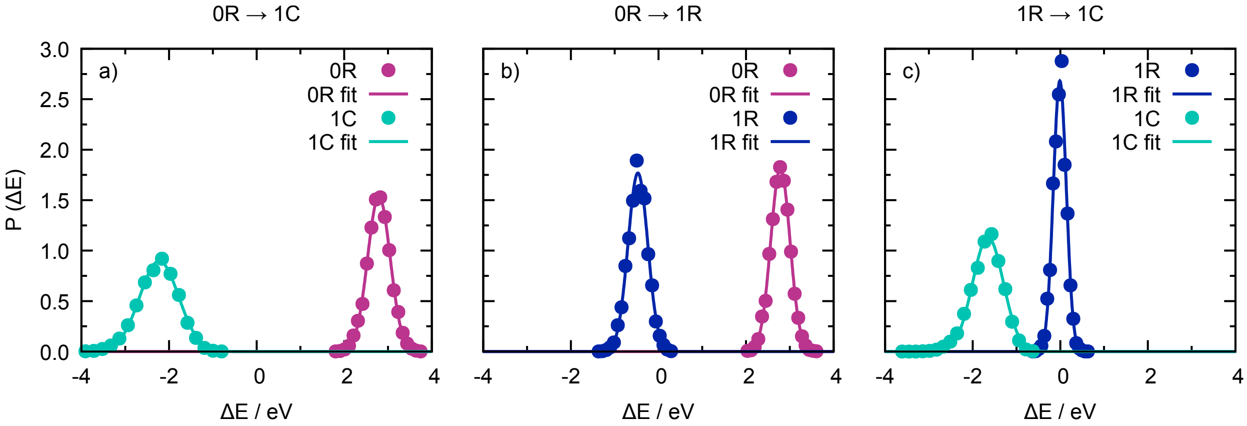

Figure 10: Normalized probability distributions of VEGs of oxidation of TEMPO in $[C_2C_1im][NTf_2]$. Points are obtained directly from MD simulations and lines are corresponding fits using the Gaussian normal distribution (eq. 2); a) the $(0R \rightarrow 1C)_{XY}$ process, where configuration space XY correspond to 0R for the rose curve and to 1C for the green; b) the $(0R \rightarrow 1R)_{XR}$ process with X equal 0 for the rose curve and 1 for the blue; c) the $(1R \rightarrow 1C)_{1Y}$ process with Y equal R for the blue curve and C for the green.

instantaneously switched from 0R to 1R state or smoothly modified using intermediate configuration spaces of 0.25R, 0.50R, and 0.75R. In both cases, the bonded part is preserved and corresponds to that of the TEMPO radical.

Histograms of the direct switches $(0R \rightarrow 1R)_{0R}$ and $(0R \rightarrow 1R)_{1R}$ are given in Fig. 10b. The distributions are Gaussian, with similar intensities and standard deviations (values given in Table S5) that points on the Marcus nature of the process. Here we intentionally did not separate inter- and intramolecular contributions in order to demonstrate that *both* non-bonded intramolecular interactions and interactions with the solute do not introduce any non-linear behavior.

From the corresponding probability distributions, Landau free energy curves can be constructed (Fig. 11). Since the edges of the histograms are never well sampled, we included the non-equilibrium points, evaluated through eq. 7, to the fit with eq. 5. Individually fitted reorganization energies of the reduced and oxidized species free energy curves, given in Table S5, are very close, that is another indicator of Marcus process. Using eq. 4 and 6, the reaction free energy and the reorganization energy of the 0R → 1R process were then computed, being equal to $\Delta A_{0R \to 1R} = 1.158\,\mathrm{eV}$ and $\lambda_{0R \to 1R} = 1.627\,\mathrm{eV}$, respectively.

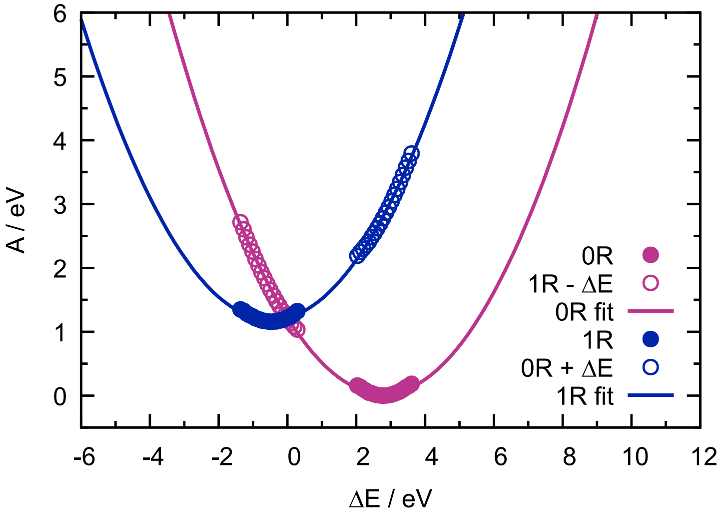

Figure 11: Landau free energies of oxidation of TEMPO in [C_2C_1im][NTf_2]. The rose curve corresponds to the free energy of 0R and the blue curve to that of 1R. Filled points are computed from the corresponding probabilities (Fig. 10b) though eq. 3, empty points though eq. 7, and lines are parabolic fits of the data points according to eq. 5.

Another confirmation of the linear response of the 0R → 1R step can be obtained on the systems with mixed Hamiltonian. The dependence of mean VEG value $\langle \Delta E(0R \to 1R)_{\eta R} \rangle$ on the coupling parameter η is shown in Fig. 12. The resulting curve is a straight line, being another evidence of Marcus response. The reaction free energy, evaluated through thermodynamic integration by eq. 11 equals $\Delta A_{0R \to 1R} = 1.185\,\mathrm{eV}$, being close to the value given in the previous paragraph.

The second step is the switch of bonded interaction parameters of TEMPO to TEMPO$^+$ while keeping the non-bonded part equal to that of the TEMPO$^+$ cation. The corresponding $(1R \to 1C)_{1R}$ and $(1R \to 1C)_{1C}$ histograms are shown in Fig 10c, being the source of a non-linear contribution to the entire 0R → 1C process. The Gaussian distribution at 1C geometry is twice wider than that at 1R geometry. The overlap of these two distributions allows us to evaluate the free energy of this step using the BAR method (eq. 12). The obtained value equals $\Delta A_{1R \to 1C} = -0.606\,\mathrm{eV}$.

Total free energy of TEMPO oxidation in [C_2C_1im][NTf_2], which is a sum of subsequent

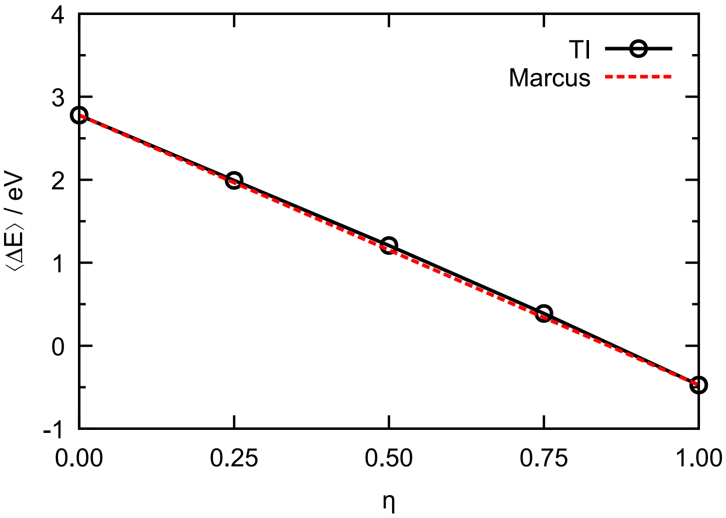

Figure 12: Average VEG of the $(0\mathrm{R} \rightarrow 1\mathrm{R})_{\eta\mathrm{R}}$ process of TEMPO oxidation in $[\mathrm{C_2C_1im}][\mathrm{NTf_2}]$ as a function of the coupling parameter η. The black curve and circles correspond to the MD simulations of the systems with the mixed Hamiltonian and the red curve to Marcus theory. The corresponding histograms are presented in Fig S11.

$0\mathrm{R} \rightarrow 1\mathrm{R}$ and $1\mathrm{R} \rightarrow 1\mathrm{C}$ steps, then reaches $\Delta A_{0\mathrm{R}\rightarrow 1\mathrm{C}} = 0.551\,\mathrm{eV}$.

An alternative pathway is $0\mathrm{R} \rightarrow 0\mathrm{C} \rightarrow 1\mathrm{C}$, in which the bonded part is changed at first, and only then the non-bonded interactions are modified. As can be seen from Fig. S10 and Table S5, the probability distributions of $(0\mathrm{R} \rightarrow 0\mathrm{C})_{0\mathrm{R}}$ and $(0\mathrm{R} \rightarrow 0\mathrm{C})_{0\mathrm{C}}$ processes are very similar to those of $(1\mathrm{R} \rightarrow 1\mathrm{C})_{1\mathrm{R}}$ and $(1\mathrm{R} \rightarrow 1\mathrm{C})_{1\mathrm{C}}$, discussed herein. The next $0\mathrm{C} \rightarrow 1\mathrm{C}$ step follows Marcus theory, similarly to $0\mathrm{R} \rightarrow 1\mathrm{R}$. The free energies of two consecutive processes are $\Delta A_{0\mathrm{R}\rightarrow 0\mathrm{C}} = -0.563\,\mathrm{eV}$ and $\Delta A_{0\mathrm{C}\rightarrow 1\mathrm{C}} = 1.098\,\mathrm{eV}$, respectively, giving a total value of $\Delta A_{0\mathrm{R}\rightarrow 1\mathrm{C}} = 0.535\,\mathrm{eV}$.

As it was shown, the non-linear effects originate from the bonded interactions of TEMPO. This is an unexpected conclusion since in the literature the most common reasons lie in a notable reorganization of the local environment of the solute upon oxidation/reduction.[44,55] For example, an increase of the coordination number of iron in the iron-water complex when passing from Fe^{2+} to Fe^{3+}.[56] In our case, the local structure of TEMPO and TEMPO^{+} indeed differs, with preferable interaction of the reduced form with an IL cation, and of the oxidized form with an IL anion. But the $0\mathrm{R} \rightarrow 1\mathrm{R}$ process, taking into account all the solvent-solute interactions, obeys Marcus theory even despite unlike microstructure. The corresponding RDFs of 0R and 1R equilibrium states are given in Fig. S13.

This 0R → 1R process is similar to the oxidation of monoatomic systems, with both intra- and intermolecular Lennard-Jones and Coulomb terms modified upon the reaction. The ET transfer reactions in ionic liquids, involving either one spherical particle or a pair spherical particles of as a probe, were extensively studied by Lynden-Bell[57–59] and Shim and Kim.[60,61] Both groups of authors suggest that Marcus theory can be in general applied to simple one-electron-transfer reactions in ILs. Lynden-Bell assumes that small deviations from non-linearity can occur due to electrostatic screening of the solute by IL ions. She underlines that non-polarizable models are unable to reproduce the high-frequency dielectric response of the IL solvent. On the other hand, a recent work of McDaniel and Yethiraj[62] proves that polarizable force fields can provide a correct dielectric constant value. This may explain why in our case an almost perfect agreement with Marcus theory is observed for the 0R → 1R step.

As was mentioned before, the non-linear 1R → 1C process comprises modification of bonded interactions upon oxidation. Significant perturbations of the intramolecular structure, such as bond breaking or formation, related to an intramolecular electron transfer, are out of the scope of Marcus theory by definition.[26,27] But our geometrical changes are rather subtle, caused by the redistribution of the electronic cloud while preserving the molecular skeleton. Indeed, even the preferable conformation of the TEMPO radical is not alerted during the reaction. The N−C−C−C dihedral distribution functions, shown in Fig. S14 remain similar in the initial 0R and the final 1C states. Thus, the main reason should lie in the shortening of the equilibrium length of the N−O bond from 1.304 Å in TEMPO to 1.207 Å in TEMPO$^+$, which is a result of a bond multiplicity change upon oxidation. The observed intramolecular geometric response to the decrease and rearrangement of electron density appears to be sufficient to violate the linear response. Nevertheless, no discussion of this delicate effect is present in the literature.

Effect of IL structure on electrochemical properties

The nature of IL ions is expected to have an important impact on the reaction free energy. We chose the hydrogen bond acidity α and the hydrogen-bond basicity β as descriptors to represent the polarity of ILs and their ability to participate in specific interactions with the solute. These are the Kamlet–Taft (KT) parameters, obtained from the UV-Vis spectral band shifts of common solvatochromic probes,[63,64]

$$XYZ = XYZ_0 + s(\pi^* + d\delta) + a\alpha + b\beta \tag{13}$$

where XYZ_0 and XYZ refer to a spectroscopic property, $s(\pi^* + d\delta)$ represents the solvent polarity-polarizability effect, and a and b are solvent-independent constants. Determination of acidity and basicity of ILs is a challenging task,[65] explaining why the literature data are rather scattered. We are using the most systematic and complete studies by Freire *et al.*[53,66] Unfortunately, they do not contain the values for some of $[\mathrm{C_2C_1im}][\mathrm{Ani}]$ ILs, so the corresponding values for $[\mathrm{C_4C_1im}][\mathrm{Ani}]$ series will be used instead. Alternatively, the authors propose to predict the KT parameters from the cation-anion hydrogen-bonding interaction energy, evaluated using the COSMO-RS method, but we aim to use only experimental values.

During the discussion below, only Marcus 0R → 1R process will be considered. The calculated free energies $\Delta A_{0\mathrm{R}\rightarrow 1\mathrm{R}}$ are given in Table 1, while corresponding histograms and Landau curves are presented in SI (Table S6, Fig. S7 and S8). This reaction free energy depends on the box size due to a different background charge applied to compensate for the non-neutrality of the simulation box containing the TEMPO^+ cation. The correcting factors, estimated using the approach of Sprik *et al.*[67] (details given in the Supporting Information), lie in the range of 0.030–0.045 eV. Since it does not have an impact on the observed trends, being an almost constant positive energy shift, we will not take it into account. The free energy of the following 1R → 1C step does not depend on the solvent ion nature, as can be seen from the comparison of the results in $[\mathrm{C_2C_1im}][\mathrm{NTf_2}]$ to those in $[\mathrm{C_2C_1im}][\mathrm{DCA}]$ and

$[C_4C_1pyrr][NTf_2]$ (Table 1, Fig. S9).

Table 1: Landau free energy (ΔA), reorganization energy (λ), activation free energy barrier ($\Delta A'$) and relative reaction rate constant (k) of TEMPO oxidation in ionic liquids

System	Process	ΔA	λ	$\Delta A'_{\mathrm{red}}$	$\log(k_{\mathrm{red}})$	$\Delta A'_{\mathrm{ox}}$	$\log(k_{\mathrm{ox}})$	Process	ΔA
$[C_2C_1im][BF_4]$	0R → 1R	1.072	1.715	1.132	−19.2	0.429	−1.02		
$[C_2C_1im][NTf_2]$	0R → 1R	1.158	1.627	1.191	−20.1	0.407	−0.57	1R → 1C	−0.606
$[C_2C_1im][DCA]$	0R → 1R	1.190	1.739	1.233	−20.9	0.435	−0.73	1R → 1C	−0.604
$[C_2C_1im][MsO]$	0R → 1R	1.243	1.776	1.283	−21.7	0.444	−0.68		
$[C_4C_1im][NTf_2]$	0R → 1R	1.368	1.686	1.383	−23.4	0.422	−0.25		
$[C_4C_1pyrr][NTf_2]$	0R → 1R	1.400	1.688	1.412	−23.9	0.422	−0.21	1R → 1C	−0.607
$[P_{4441}][NTf_2]$	0R → 1R	1.490	1.732	1.498	−25.3	0.433	−0.14		
$[C_8C_1im][NTf_2]$	0R → 1R	1.532	1.736	1.538	−26.0	0.434	−0.10		

Energies are given in eV. Standard deviations are typically below 0.01 eV.

The reaction free energy $\Delta A_{0R\to 1R}$ increases in the row $BF_4^- < NTf_2^- < DCA^- < MsO^-$ that can be roughly correlated with the basicity of the anions (Fig. 13a). A more basic ion, such as mesylate, forms stable complexes both with $C_2C_1im^+$ and $TEMPO^+$. The competition between [IL cation ... anion] and [$TEMPO^+$ cation ... anion] interactions play a dominant role, increasing the free energy. On the contrary, a bulky NTf_2^- anion with the delocalized charge gives weaker H-bonds with both species and consequently lower free energy. Similar conclusions were reached by Delorme *et al.*,[4] who suggested that for ILs with $\beta > 0.5$, the midpoint potential of TEMPO oxidation ($E_{1/2} \approx -\Delta A - E_{\mathrm{ref}}$, where E_{ref} is the reference potential) decreases linearly when β increases. Unfortunately, it is not possible to perform a quantitative comparison between our simulations and these experimental results, since in the latter there is no common reference electrode (the same couple is used as a pseudo-reference, but the solvent differs from one system to another), hence different reference potentials E_{ref} are used for each solvent.

A much better correlation with the basicity of the anion is observed for reorganization energies, shown in Fig. 13b. Stronger interactions of the solute with the solvent require greater energies to rearrange its microenvironment as a response to the oxidation/reduction process. Unlike the previous case, greater energy is needed for the BF_4^- system than for the

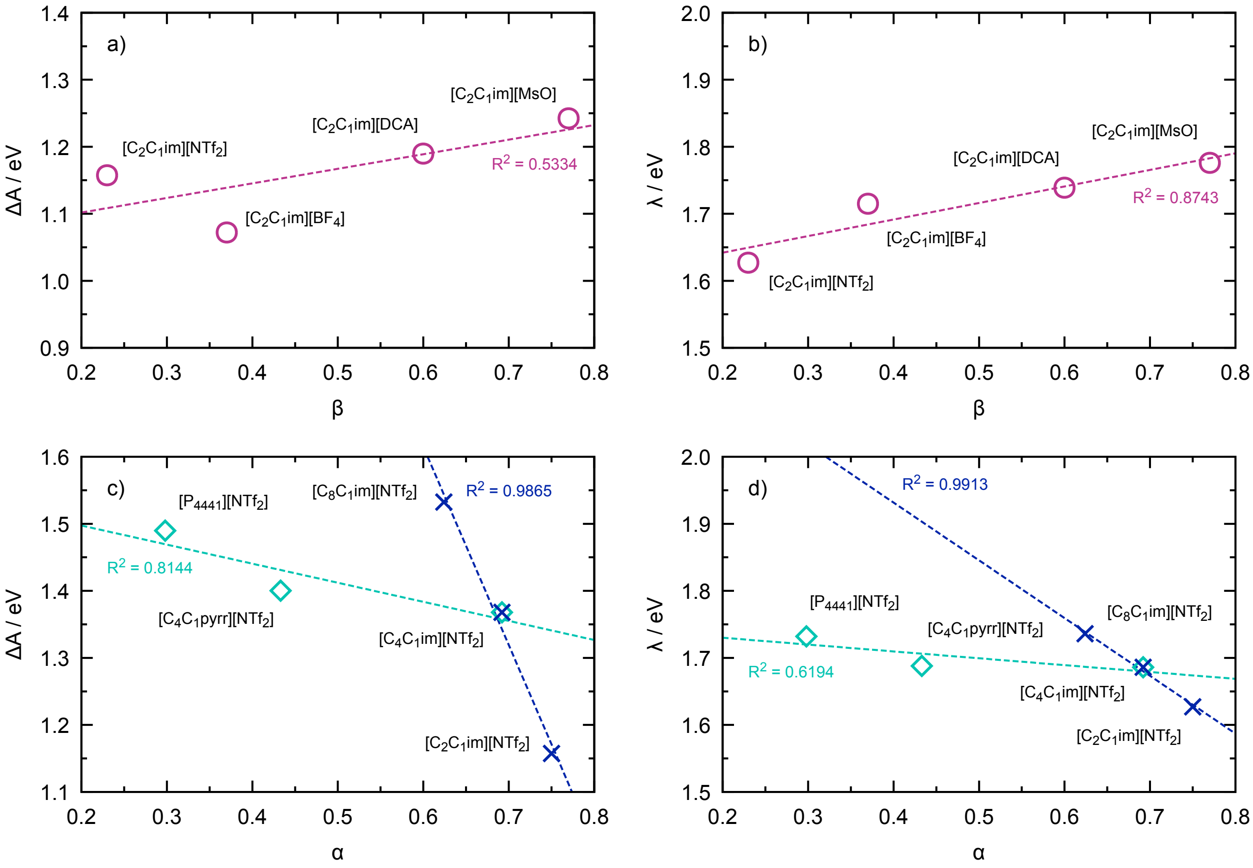

Figure 13: Correlation between the reaction free energy (a,c) and the reorganization free energy (b,d) with the basicity of the anion β[53] (a,b) and the acidity of the cation α[66] (c,d). Due to the absence of the literature data on basicity of some $[C_2C_1im][Ani]$ ILs, corresponding values for $[C_4C_1im][Ani]$ series were considered. Rose circles correspond to the series of anions, $[C_2C_1im][Ani]$; turquoise diamonds to the series of cations with different head groups, $[Cat][NTf_2]$; blue crosses to the series of imidazolium cations with different side chain lengths, $[C_nC_1im][NTf_2]$. Dashed lines are linear fits of points of the corresponding colors with given coefficients of determination R^2.

NTf_2^-. It can be explained by the higher flexibility of bistriflimide, which allows an easier transition from the local structure of TEMPO to that of $TEMPO^+$.

The nature of the IL cation also has an impact on the electrochemical properties, being similar by magnitude to that of the anion. The reaction free energy is inversely proportional to hydrogen-bond donating ability (Fig. 13c), following the sequence of $C_4C_1im^+ < C_4C_1pyrr^+ < P_{4441}^+$. Since H-bonds of the imidazolium cation are stronger than those of phosphonium, it is more favorable for the imidazolium to leave the complex with TEMPO radical and benefit from forming a cation-anion IL pair. This results in lowering free energies of oxidation in more acid ILs. A similar trend in oxidation potential was observed in the QM study by Wylie *et al.*[18]

Nevertheless, the acidity of the cation cannot be considered a prevailing factor when analyzing reorganization energies. Despite a significant difference in the H-bond donating ability, the λ-values for imidazolium and pyrrolidinium ILs, given in Table 1, are identical, and greater energy is required only for a phosphonium IL. The coefficient of determination in this case (Fig. 13d) drops down notably when compared to that for reaction free energies. This points at a major role of steric effects in the rearrangement of the microenvironment of TEMPO rather than that of specific [TEMPO radical ... IL cation] interactions.

Elongation of the side chain from ethyl to octyl in the sequence $C_2C_1im^+ < C_4C_1im^+ < C_8C_1im^+$ also augments the free energy, by approximately 0.05–0.10 eV per each extra methylene group. As seen from Fig. 13c, a decrease in the cation acidity linearly follows an increase of the side chain length, with the determination coefficient close to 1. This excellent correlation is also observed for the reorganization energies (Fig. 13d), though the energy difference per extra methylene group drops to 0.010–0.025 eV, becoming almost negligible.

We have shown that the electrochemical properties of TEMPO strongly depend on the nature of an ionic liquid, namely on the acidity and the basicity of its ions. By combining bulky cations with basic anions, the potential can be lowered, while the use of small acid cations and hydrophobic anions results in higher values, favoring the reaction from the thermodynamic point of view.

Kinetics of oxidation/reduction

Though in the previous section we focused only on the TEMPO/TEMPO$^+$ oxidation reaction, here the kinetics of the oxidation and the reduction should be discussed separately. The activation free energy $\Delta A'$, evaluated through eq. 8, is a function of the reaction free energy taken with an opposite sign and known as a driving force $-\Delta A$, which depends on the direction of the redox process. Note that our calculations correspond to a null chemical potential for the electron. When it takes a finite value, the free energy curves such as the ones shown on Fig 11 will be accordingly shifted, and so will the activation free energy. However, it remains possible to estimate relative rate constants under null electron chemical potential conditions since the trend among ionic liquids should remain unchanged. Relative rates were evaluated though eq. 9, by setting the exponential prefactor $\mathcal{A}$ to 1. The resulting values of k_{ox} and k_{red} are given in Table 1 on a logarithmic scale.

The rate constant of the TEMPO oxidation follows the next trend: higher is the driving force, faster is the reaction. This is the signature of the direct Marcus region taking place when the reaction free energy is smaller than the reorganization energy.[68,69] The corresponding plot is given in Fig. 14, with the maximum matching the average value of the reorganization energies across all the systems. In the case of TEMPO^+ reduction, the points approach the activationless electron transfer region, in which the reduction driving force is approximately equal to the reorganization energy. The reaction then becomes close to barrierless, with diffusion-limited kinetics.[70,71] No systems belonging to the inverted region when $-\Delta A$ exceeds λ were found.

The influence of the IL nature on the kinetics appears to be different for TEMPO oxidation and TEMPO^+ reduction. In the first case, the reaction rates follow the exact trend of the reaction free energy. The values roughly increase with a decrease of the basicity of the anion, from MsO^- to BF_4^-, with an enhancement of the acidity of a cationic head group, from phosphonium to imidazolium, and with shortening of its side chain, from octyl to ethyl.

Contrary to the previous case, the rate of the TEMPO^+ reduction is higher in the systems composed of a large cation with a long non-polar side chain combined with the NTf_2^- anion. This anion stabilises TEMPO^+ *less* than more basic DCA^- or MsO^-, allowing it to participate in the redox cycle. The same conclusions were made by Delorme *et al.*,[4] who showed that the benzyl alcohol oxidation by TEMPO^+ was faster in $[\mathrm{C_8C_1im}][\mathrm{NTf_2}]$ than in $[\mathrm{C_8C_1im}][\mathrm{DCA}]$, which is in accordance with our results for $\mathrm{C_2C_1im}^+$-based systems. Nevertheless, we do not

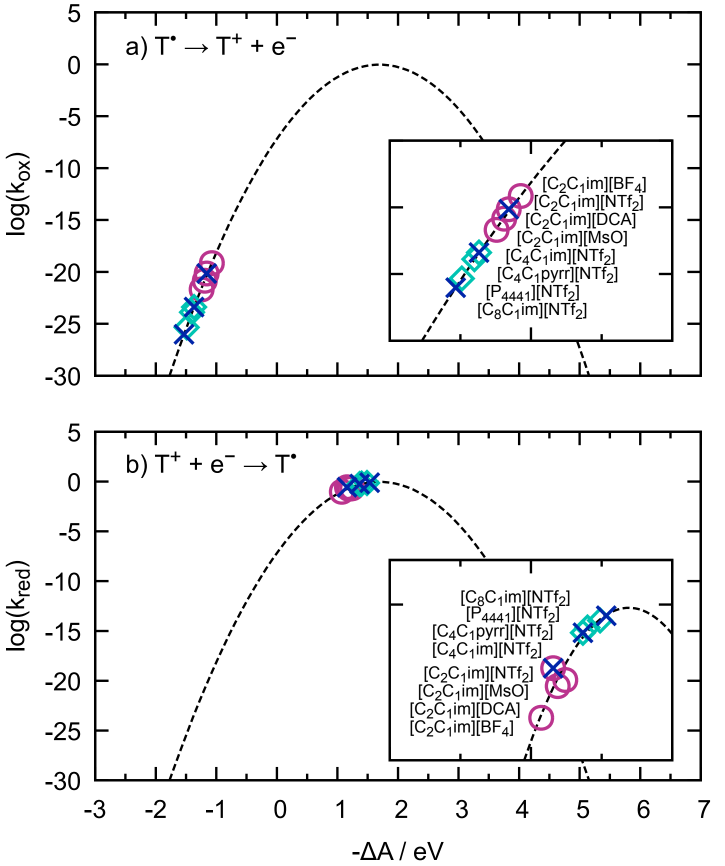

Figure 14: The relative reaction rate constants (k) of TEMPO oxidation (a) and TEMPO$^+$ reduction (b) as a function of the driving force, for a null electron chemical potential. Rose circles correspond to the series of anions, [C$_2$C$_1$im][Ani]; turquoise diamonds to the series of cations with different head groups, [Cat][NTf$_2$]; blue crosses to the series of imidazolium cations with different side chain lengths, [C$_\text{n}$C$_1$im][NTf$_2$]. The dashed line represents a fit performed on the full set of points.

observe a perfect agreement with the experimental trends. In particular, the measured rates of benzyl alcohol oxidation are greater in phosphonium, ammonium, and pyrrolidinium ILs than in imidazolium ones. This can be explained by a specific interaction, $\pi - \pi$ stacking between the imidazolium ring and the aromatic system of the alcohol. In our case, the limiting factors due to the presence of a third component are obviously not considered.

While the nature of the IL ions determines the activation barrier, another important parameter is the viscosity which limits mass and electron transfer.[72] For example, Minteer *et al.*[17] demonstrated that the peak current in cyclic voltammetry of a TEMPO derivative drastically diminished and the peak-to-peak separation increased in more viscous [$C_{10}C_1$im][NTf_2] than in more fluid [C_4C_1im][NTf_2]. Indeed, the rate constant of TEMPO oxidation, shown in Fig. 15a, decreases with an elongation of the imidazolium side chain. On the other hand, no correlation is observed for the imidazolium family with a set of different anions, where interactions of $TEMPO^+$ with the anion become more important than the viscosity impact. The latter is also true for the $TEMPO^+$ reduction process, for which higher rates are observed for ILs with a low-interacting NTf_2^- anion, while viscosity varies significantly as a function of the cationic head group (Fig. 15b). Thus, when choosing an IL as a solvent for TEMPO-mediated reactions viscosity should be taken into account as an independent factor, poorly correlated with ionic nature.

Therefore, by combining different cations and anions of ILs we can control the reactivity of TEMPO and $TEMPO^+$ in the redox processes. The kinetics can be tuned by changing the acid-base character of the solvent ions as well as the viscosity of a solvent. Based on both factors, one should consider low-viscous NTf_2^--based ionic liquids with small imidazolium cations as the most promising reaction medium.

Conclusions

In the present paper, we studied the process of TEMPO oxidation from energetic, kinetic, and structural points of view. First, we revealed that the reduced and the oxidized forms of TEMPO have different solvation environments, with the main trends preserved for all ionic solvents studied. The TEMPO radical prefers to interact with an IL cation through the formation of H-bonds *via* its nitroxide group with acid hydrogen atoms of cationic head groups. In addition, elongation of the alkyl side chain of the cation leads to appearing of dispersive interactions with methyl groups of TEMPO. Upon oxidation, the IL cation is repelled from $TEMPO^+$, and the latter forms weak H-bonds through its hydrogen atoms with acceptor atoms of the anions.

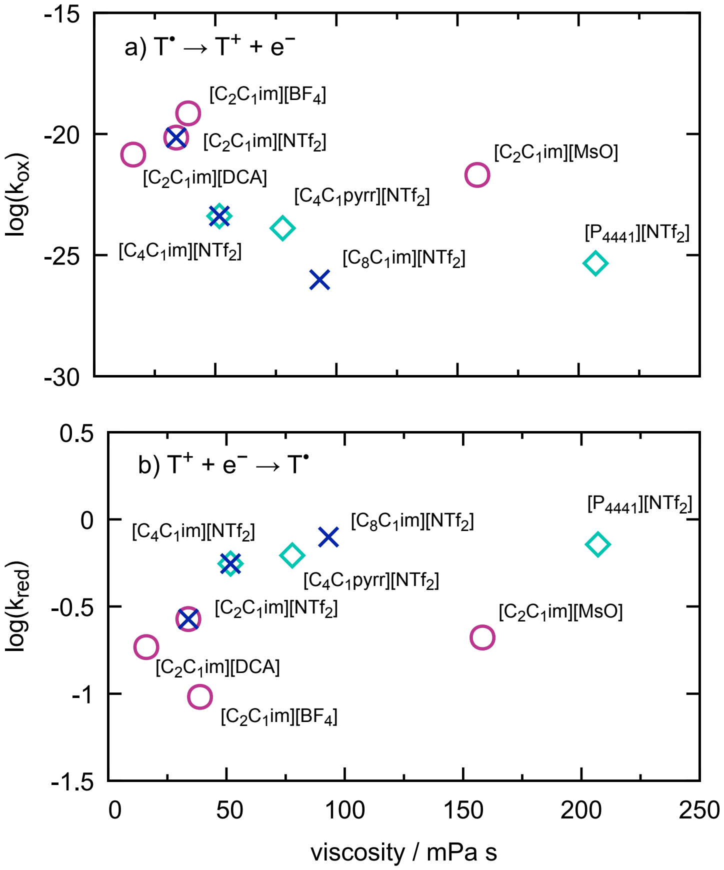

Figure 15: The relative reaction rate constants (k) of TEMPO oxidation (a) and TEMPO$^+$ reduction (b) as a function of viscosity of ILs.[73–77] Rose circles correspond to the series of anions, $[C_2C_1im][Ani]$; turquoise diamonds to the series of cations with different head groups, $[Cat][NTf_2]$; blue crosses to the series of imidazolium cations with different side chain lengths, $[C_nC_1im][NTf_2]$.

The electrochemistry of oxidation of TEMPO, in general, does not follow Marcus theory. This violation rises from the changes in intramolecular bonded potential, caused by the redistribution of partial charges in the solute during the reaction. However, this effect can be eliminated due to its independence from the solvent nature. Then, the change in non-bonded Coulomb and van der Waals potentials can be analyzed in the frame of Marcus theory, and the reaction free energies of the process in different ILs can be compared. The values were shown to be correlated with the acidity of the cation and the basicity of the anion. Similar trends were observed for the reorganization energy.

The acidic character of IL ions affects the kinetics of the process. Higher reaction rates of TEMPO oxidation are observed for ILs composed of small imidazolium-based cations and hydrophobic anions with low basicity. On the contrary, TEMPO^+ reduction is favored by the presence of bulky cations with lower acidity. These effects are a result of a tight balance of solute-solvent interactions, providing an optimum rate of stabilization of TEMPO and TEMPO^+ in the solution. Among the above recommended solvents, low-viscous ILs should be considered as the most preferable choice due to the enhanced mass and electron transfer.

Acknowledgement

This work was funded by European Research Council (ERC) under the European Union's Horizon 2020 research and innovation program (grant agreement 771294). Computational tasks were performed using resources from GENCI-IDRIS (Grants 2021-A0100910463 and 2022-A0120910463). The authors thank Guillaume Jeanmairet for the fruitful discussion.

References

1. Vogler, T.; Studer, A. Applications of TEMPO in Synthesis. *Synthesis* **2008**, *2008*, 1979–1993, DOI: `10.1055/s-2008-1078445`.

2. Nutting, J. E.; Rafiee, M.; Stahl, S. S. Tetramethylpiperidine N-Oxyl (TEMPO), Phthalimide N-Oxyl (PINO), and Related N-Oxyl Species: Electrochemical Properties and Their Use in Electrocatalytic Reactions. *Chem. Rev.* **2018**, *118*, 4834–4885, DOI: `10.1021/acs.chemrev.7b00763`.

3. Beejapur, H. A.; Zhang, Q.; Hu, K.; Zhu, L.; Wang, J.; Ye, Z. TEMPO in Chemical Transformations: From Homogeneous to Heterogeneous. *ACS Catal.* **2019**, *9*, 2777–2830, DOI: `10.1021/acscatal.8b05001`.

4. Delorme, A. E.; Sans, V.; Licence, P.; Walsh, D. A. Tuning the Reactivity of TEMPO during Electrocatalytic Alcohol Oxidations in Room-Temperature Ionic Liquids. *ACS Sustain. Chem. Eng.* **2019**, *7*, 11691–11699, DOI: `10.1021/acssuschemeng.9b01823`.

5. Bergner, B. J.; Schürmann, A.; Peppler, K.; Garsuch, A.; Janek, J. TEMPO: A Mobile Catalyst for Rechargeable Li-O2 Batteries. *J. Am. Chem. Soc.* **2014**, *136*, 15054–15064, DOI: `10.1021/ja508400m`.

6. Winsberg, J.; Stolze, C.; Muench, S.; Liedl, F.; Hager, M. D.; Schubert, U. S. TEMPO/Phenazine Combi-Molecule: A Redox-Active Material for Symmetric Aqueous Redox-Flow Batteries. *ACS Energy Lett.* **2016**, *1*, 976–980, DOI: `10.1021/acsenergylett.6b00413`.

7. Liu, Y.; Goulet, M.-A.; Tong, L.; Liu, Y.; Ji, Y.; Wu, L.; Gordon, R. G.; Aziz, M. J.; Yang, Z.; Xu, T. A Long-Lifetime All-Organic Aqueous Flow Battery Utilizing TMAP-TEMPO Radical. *Chem* **2019**, *5*, 1861–1870, DOI: `10.1016/j.chempr.2019.04.021`.

8. Mourad, E.; Coustan, L.; Lannelongue, P.; Zigah, D.; Mehdi, A.; Vioux, A.; Freunberger, S. A.; Favier, F.; Fontaine, O. Biredox ionic liquids with solid-like redox density in the liquid state for high-energy supercapacitors. *Nat. Mater.* **2017**, *16*, 446–453, DOI: `10.1038/nmat4808`.

9. Keana, J. F. W. Newer aspects of the synthesis and chemistry of nitroxide spin labels. *Chem. Rev.* **1978**, *78*, 37–64, DOI: `10.1021/cr60311a004`.

10. Jiang, W.-L.; Peng, Z.; Huang, B.; Zhao, X.-L.; Sun, D.; Shi, X.; Yang, H.-B. TEMPO Radical-Functionalized Supramolecular Coordination Complexes with Controllable Spin–Spin Interactions. *J. Am. Chem. Soc.* **2021**, *143*, 433–441, DOI: `10.1021/jacs.0c11738`.

11. Isogai, A.; Saito, T.; Fukuzumi, H. TEMPO-oxidized cellulose nanofibers. *Nanoscale* **2011**, *3*, 71–85, DOI: `10.1039/C0NR00583E`.

12. Kisszekelyi, P.; Hardian, R.; Vovusha, H.; Chen, B.; Zeng, X.; Schwingenschlögl, U.; Kupai, J.; Szekely, G. Selective Electrocatalytic Oxidation of Biomass-Derived 5-Hydroxymethylfurfural to 2,5-Diformylfuran: from Mechanistic Investigations to Catalyst Recovery. *ChemSusChem* **2020**, *13*, 3127–3136, DOI: `10.1002/cssc.202000453`.

13. Deng, J.; Ben Tayeb, K.; Dong, C.; Simon, P.; Marinova, M.; Dubois, M.; Morin, J.-C.; Zhou, W.; Capron, M.; Ordomsky, V. V. TEMPO-Ru-BEA Composite Material for the Selective Oxidation of Alcohols to Aldehydes. *ACS Catal.* **2022**, *12*, 8925–8935, DOI: `10.1021/acscatal.2c01554`.

14. Welton, T. Room-Temperature Ionic Liquids. Solvents for Synthesis and Catalysis. *Chem. Rev.* **1999**, *99*, 2071–2084, DOI: `10.1021/cr980032t`.

15. Plechkova, N. V.; Seddon, K. R. Applications of ionic liquids in the chemical industry. *Chem. Soc. Rev.* **2008**, *37*, 123–150, DOI: `10.1039/B006677J`.

16. Hallett, J. P.; Welton, T. Room-Temperature Ionic Liquids: Solvents for Synthesis and Catalysis. 2. *Chem. Rev.* **2011**, *111*, 3508–3576, DOI: `10.1021/cr1003248`.

17. Li, M.; Klunder, K.; Blumenthal, E.; Prater, M. B.; Lee, J.; Matthiesen, J. E.; Minteer, S. D. Ionic Liquid Stabilized 2,2,6,6-Tetramethylpiperidine 1-Oxyl Catalysis for Alcohol Oxidation. *ACS Sustain. Chem. Eng.* **2020**, *8*, 4489–4498, DOI: `10.1021/acssuschemeng.9b07650`.

18. Wylie, L.; Oyaizu, K.; Karton, A.; Yoshizawa-Fujita, M.; Izgorodina, E. I. Toward Improved Performance of All-Organic Nitroxide Radical Batteries with Ionic Liquids: A Theoretical Perspective. *ACS Sustain. Chem. Eng.* **2019**, *7*, 5367–5375, DOI: `10.1021/acssuschemeng.8b06393`.

19. Wylie, L.; Seeger, Z. L.; Hancock, A. N.; Izgorodina, E. I. Increased stability of nitroxide radicals in ionic liquids: more than a viscosity effect. *Phys. Chem. Chem. Phys.* **2019**, *21*, 2882–2888, DOI: `10.1039/C8CP04854A`.

20. Wylie, L.; Blesch, T.; Freeman, R.; Hatakeyama-Sato, K.; Oyaizu, K.; Yoshizawa-Fujita, M.; Izgorodina, E. I. Reversible Reduction of the TEMPO Radical: One Step Closer to an All-Organic Redox Flow Battery. *ACS Sustain. Chem. Eng.* **2020**, *8*, 17988–17996, DOI: `10.1021/acssuschemeng.0c05687`.

21. Wylie, L.; Hakatayama-Sato, K.; Go, C.; Oyaizu, K.; Izgorodina, E. I. Electrochemical characterization and thermodynamic analysis of TEMPO derivatives in ionic liquids. *Phys. Chem. Chem. Phys.* **2021**, *23*, 10205–10217, DOI: `10.1039/D0CP05350C`.

22. Zhang, S.; Wang, G.; Lu, Y.; Zhu, W.; Peng, C.; Liu, H. The Interactions between Imidazolium-Based Ionic Liquids and Stable Nitroxide Radical Species: A Theoretical Study. *J. Phys. Chem. A* **2016**, *120*, 6089–6102, DOI: `10.1021/acs.jpca.6b05770`.

23. Strehmel, V. Radicals in Ionic Liquids. *ChemPhysChem* **2012**, *13*, 1649–1663, DOI: `10.1002/cphc.201100982`.

24. Strehmel, V.; Berdzinski, S.; Rexhausen, H. Interactions between ionic liquids and radicals. *J. Mol. Liq.* **2014**, *192*, 153–170, DOI: `10.1016/j.molliq.2013.12.007`.

25. Bedrov, D.; Piquemal, J.-P.; Borodin, O.; MacKerell, A. D.; Roux, B.; Schröder, C. Molecular Dynamics Simulations of Ionic Liquids and Electrolytes Using Polarizable Force Fields. *Chem. Rev.* **2019**, *119*, 7940–7995, DOI: `10.1021/acs.chemrev.8b00763`.

26. Marcus, R. A. On the Theory of Oxidation-Reduction Reactions Involving Electron Transfer. I. *J. Chem. Phys.* **1956**, *24*, 966–978, DOI: `10.1063/1.1742723`.

27. Marcus, R. A. On the Theory of Electron-Transfer Reactions. VI. Unified Treatment for Homogeneous and Electrode Reactions. *J. Chem. Phys.* **1965**, *43*, 679–701, DOI: `10.1063/1.1696792`.

28. Eastman, P.; Swails, J.; Chodera, J. D.; McGibbon, R. T.; Zhao, Y.; Beauchamp, K. A.; Wang, L.-P.; Simmonett, A. C.; Harrigan, M. P.; Stern, C. D.; Wiewiora, R. P.;

Brooks, B. R.; Pande, V. S. OpenMM 7: Rapid development of high performance algorithms for molecular dynamics. *PLoS Comput. Biol.* **2017**, *13*, e1005659, DOI: `10.1371/journal.pcbi.1005659`.

29. Martínez, L.; Andrade, R.; Birgin, E. G.; Martínez, J. M. PACKMOL: A package for building initial configurations for molecular dynamics simulations. *J. Comp. Chem.* **2009**, *30*, 2157–2164, DOI: `10.1002/jcc.21224`.
30. Padua, A. A. H. github.com/paduagroup/fftool. 2021; `https://github.com/paduagroup/fftool`.
31. Lamoureux, G.; Roux, B. Modeling induced polarization with classical Drude oscillators: Theory and molecular dynamics simulation algorithm. *J. Chem. Phys.* **2003**, *119*, 3025–3039.
32. Thole, B. T. Molecular polarizabilities calculated with a modified dipole interaction. *Chem. Phys.* **1981**, *59*, 341–350, DOI: `10.1016/0301-0104(81)85176-2`.
33. Noskov, S. Y.; Lamoureux, G.; Roux, B. Molecular dynamics study of hydration in ethanol-water mixtures using a polarizable force field. *J. Phys. Chem. B* **2005**, *109*, 6705–6713, DOI: `10.1021/ct600180x`.
34. Huang, J.; Lemkul, J. A.; Eastman, P. K.; MacKerell Jr., A. D. Molecular dynamics simulations using the drude polarizable force field on GPUs with OpenMM: Implementation, validation, and benchmarks. *J. Comput. Chem.* **2018**, *39*, 1682–1689, DOI: `10.1002/jcc.25339`.
35. Goloviznina, K.; Canongia Lopes, J. N.; Costa Gomes, M.; Pádua, A. A. H. Transferable, Polarizable Force Field for Ionic Liquids. *J. Chem. Theory Comput.* **2019**, *15*, 5858–5871, DOI: `10.1021/acs.jctc.9b00689`.

36. Goloviznina, K.; Gong, Z.; Costa Gomes, M. F.; Pádua, A. A. H. Extension of the CL&Pol Polarizable Force Field to Electrolytes, Protic Ionic Liquids, and Deep Eutectic Solvents. *J. Chem. Theory Comput.* **2021**, *17*, 1606–1617, DOI: `10.1021/acs.jctc.0c01002`.

37. Goloviznina, K.; Gong, Z.; Padua, A. A. H. The CL&Pol polarizable force field for the simulation of ionic liquids and eutectic solvents. *Wiley Interdiscip. Rev. Comput. Mol. Sci.* **2022**, *12*, e1572, DOI: `10.1002/wcms.1572`.

38. Berthin, R.; Serva, A.; Reeves, K. G.; Heid, E.; Schröder, C.; Salanne, M. Solvation of anthraquinone and TEMPO redox-active species in acetonitrile using a polarizable force field. *J. Chem. Phys.* **2021**, *155*, 074504, DOI: `10.1063/5.0061891`.

39. Brehm, M.; Kirchner, B. TRAVIS - A Free Analyzer and Visualizer for Monte Carlo and Molecular Dynamics Trajectories. *J. Chem. Inf. Model.* **2011**, *51*, 2007–2023, DOI: `10.1021/ci200217w`.

40. Brehm, M.; Thomas, M.; Gehrke, S.; Kirchner, B. TRAVIS—A free analyzer for trajectories from molecular simulation. *J. Chem. Phys.* **2020**, *152*, 164105, DOI: `10.1063/5.0005078`.

41. Humphrey, W.; Dalke, A.; Schulten, K. VMD: Visual molecular dynamics. *J. Mol. Graph.* **1996**, *14*, 33–38, DOI: `10.1016/0263-7855(96)00018-5`.

42. Warshel, A. Dynamics of Reactions in Polar Solvents. Semiclassical Trajectory Studies of Electron-Transfer and Proton-Transfer Reactions. *J. Phys. Chem.* **1982**, *86*, 2218–2224.

43. Zwickl, J.; Shenvi, N.; Schmidt, J. R.; Tully, J. C. Transition State Barriers in Multidimensional Marcus Theory. *J. Phys. Chem. A* **2008**, *112*, 10570–10579, DOI: `10.1021/jp805065g`.

44. Blumberger, J. Recent Advances in the Theory and Molecular Simulation of Biological Electron Transfer Reactions. *Chem. Rev.* **2015**, *115*, 11191–11238, DOI: `10.1021/acs.chemrev.5b00298`.

45. Vuilleumier, R.; Tay, K. A.; Jeanmairet, G.; Borgis, D.; Boutin, A. Extension of Marcus Picture for Electron Transfer Reactions with Large Solvation Changes. *J. Am. Chem. Soc.* **2012**, *134*, 2067–2074, DOI: `10.1021/ja2069104`.

46. Reeves, K. G.; Serva, A.; Jeanmairet, G.; Salanne, M. A first-principles investigation of the structural and electrochemical properties of biredox ionic species in acetonitrile. *Phys. Chem. Chem. Phys.* **2020**, *22*, 10561–10568, DOI: `10.1039/C9CP06658F`.

47. Bennett, C. H. Efficient estimation of free energy differences from Monte Carlo data. *J. Comput. Phys.* **1976**, *22*, 245–268, DOI: `10.1016/0021-9991(76)90078-4`.

48. Hunt, P. A.; Ashworth, C. R.; Matthews, R. P. Hydrogen bonding in ionic liquids. *Chem. Soc. Rev.* **2015**, *44*, 1257–1288, DOI: `10.1039/C4CS00278D`.

49. Morco, R. P.; Musa, A. Y.; Wren, J. C. The molecular structures and the relationships between the calculated molecular and observed bulk phase properties of phosphonium-based ionic liquids. *Solid State Ion.* **2014**, *258*, 74–81, DOI: `10.1016/j.ssi.2014.02.004`.

50. Hunt, P. A.; Gould, I. R. Structural Characterization of the 1-Butyl-3-methylimidazolium Chloride Ion Pair Using ab Initio Methods. *J. Phys. Chem. A* **2006**, *110*, 2269–2282, DOI: `10.1021/jp0547865`.

51. Shiflett, M. B.; Kasprzak, D. J.; Junk, C. P.; Yokozeki, A. Phase behavior of {carbon dioxide+[bmim][Ac]} mixtures. *The Journal of Chemical Thermodynamics* **2008**, *40*, 25–31, DOI: `10.1016/j.jct.2007.06.003`.

52. Chaban, V. V. Carbon Dioxide Chemisorption by Ammonium and Phosphonium Ionic Liquids: Quantum Chemistry Calculations. *J. Phys. Chem. B* **2022**, *126*, 5497–5506, DOI: `10.1021/acs.jpcb.2c02968`.

53. Cláudio, A. F. M.; Swift, L.; Hallett, J. P.; Welton, T.; Coutinho, J. A. P.; Freire, M. G. Extended scale for the hydrogen-bond basicity of ionic liquids. *Phys. Chem. Chem. Phys.* **2014**, *16*, 6593–6601, DOI: `10.1039/C3CP55285C`.

54. Evans, R. G.; Wain, A. J.; Hardacre, C.; Compton, R. G. An electrochemical and ESR spectroscopic study on the molecular dynamics of TEMPO in room temperature ionic liquid solvents. *Chemphyschem* **2005**, *6*, 1035–1039, DOI: `10.1002/cphc.200500157`.

55. Oberhofer, H.; Reuter, K.; Blumberger, J. Charge Transport in Molecular Materials: An Assessment of Computational Methods. *Chem. Rev.* **2017**, *117*, 10319–10357, DOI: `10.1021/acs.chemrev.7b00086`.

56. Li, Z.; Jeanmairet, G.; Méndez-Morales, T.; Burbano, M.; Haefele, M.; Salanne, M. Confinement Effects on an Electron Transfer Reaction in Nanoporous Carbon Electrodes. *J. Phys. Chem. Lett.* **2017**, *8*, 1925–1931, DOI: `10.1021/acs.jpclett.7b00458`.

57. Lynden-Bell, R. M. Can Marcus Theory Be Applied to Redox Processes in Ionic Liquids? A Comparative Simulation Study of Dimethylimidazolium Liquids and Acetonitrile. *J. Phys. Chem. B* **2007**, *111*, 10800–10806, DOI: `10.1021/jp074298s`.

58. Lynden-Bell, R. M. Does Marcus theory apply to redox processes in ionic liquids? A simulation study. *Electrochem. commun.* **2007**, *9*, 1857–1861, DOI: `10.1016/j.elecom.2007.04.010`.

59. Lynden-Bell, R. M. Redox potentials and screening in ionic liquids: Effects of sizes and shapes of solute ions. *Chem. Phys.* **2008**, *129*, 204503, DOI: `10.1063/1.3020439`.

60. Shim, Y.; Kim, H. J. Free Energy and Dynamics of Electron-Transfer Reactions in a Room Temperature Ionic Liquid. *J. Phys. Chem. B* **2007**, *111*, 4510–4519, DOI: `10.1021/jp9065407`.

61. Shim, Y.; Kim, H. J. Adiabatic Electron Transfer in a Room-Temperature Ionic Liquid: Reaction Dynamics and Kinetics. *J. Phys. Chem. B* **2009**, *113*, 12964–12972, DOI: `10.1021/jp9065407`.

62. McDaniel, J. G.; Yethiraj, A. Influence of Electronic Polarization on the Structure of Ionic Liquids. *J. Phys. Chem. Lett.* **2018**, *9*, 4765–4770, DOI: `10.1021/acs.jpclett.8b02120`.

63. Kamlet, M. J.; Taft, R. W. The solvatochromic comparison method. I. The .beta.-scale of solvent hydrogen-bond acceptor (HBA) basicities. *J. Am. Chem. Soc.* **1976**, *98*, 377–383, DOI: `10.1021/ja00418a009`.

64. Taft, R. W.; Kamlet, M. J. The solvatochromic comparison method. 2. The .alpha.-scale of solvent hydrogen-bond donor (HBD) acidities. *J. Am. Chem. Soc.* **1976**, *98*, 2886–2894, DOI: `10.1021/ja00426a036`.

65. Ab Rani, M. A.; Brant, A.; Crowhurst, L.; Dolan, A.; Lui, M.; Hassan, N. H.; Hallett, J. P.; Hunt, P. A.; Niedermeyer, H.; Perez-Arlandis, J. M.; Schrems, M.; Welton, T.; Wilding, R. Understanding the polarity of ionic liquids. *Phys. Chem. Chem. Phys.* **2011**, *13*, 16831–16840, DOI: `10.1039/C1CP21262A`.

66. Kurnia, K. A.; Lima, F.; Cláudio, A. F. M.; Coutinho, J. A. P.; Freire, M. G. Hydrogen-bond acidity of ionic liquids: an extended scale. *Phys. Chem. Chem. Phys.* **2015**, *17*, 18980–18990, DOI: `10.1039/C5CP03094C`.

67. Ayala, R.; Sprik, M. A Classical Point Charge Model Study of System Size Dependence of Oxidation and Reorganization Free Energies in Aqueous Solution. *J. Phys. Chem. B* **2008**, *112*, 257–269, DOI: `10.1021/jp0748516`.

68. Marcus, R. A.; Sutin, N. Electron transfers in chemistry and biology. *Biochimica et Biophysica Acta (BBA) - Reviews on Bioenergetics* **1985**, *811*, 265–322, DOI: `10.1016/0304-4173(85)90014-X`.

69. Miller, J. R.; Calcaterra, L. T.; Closs, G. L. Intramolecular long-distance electron transfer in radical anions. The effects of free energy and solvent on the reaction rates. *J. Am. Chem. Soc.* **1984**, *106*, 3047–3049, DOI: `10.1021/ja00322a058`.

70. Grampp, G. The Marcus Inverted Region from Theory to Experiment. *Angew. Chem., Int. Ed. Engl.* **1993**, *32*, 691–693, DOI: `10.1002/anie.199306911`.

71. Turró, C.; Zaleski, J. M.; Karabatsos, Y. M.; Nocera, D. G. Bimolecular Electron Transfer in the Marcus Inverted Region. *J. Am. Chem. Soc.* **1996**, *118*, 6060–6067, DOI: `10.1021/ja960575p`.

72. Skrzypczak, A.; Neta, P. Diffusion-Controlled Electron-Transfer Reactions in Ionic Liquids. *J. Phys. Chem. A* **2003**, *107*, 7800–7803, DOI: `10.1021/jp030416+`.

73. Neves, C. M. S. S.; Kurnia, K. A.; Coutinho, J. A. P.; Marrucho, I. M.; Lopes, J. C.; Freire, M. G.; Rebelo, L. P. N. Systematic Study of the Thermophysical Properties of Imidazolium-Based Ionic Liquids with Cyano-Functionalized Anions. *J. Phys. Chem. B* **2013**, *117*, 10271–10283, DOI: `10.1021/jp405913b`.

74. Tariq, M.; Carvalho, P. J.; Coutinho, J. A. P.; Marrucho, I. M.; Lopes, J. C.; Rebelo, L. P. N. Viscosity of (C2–C14) 1-alkyl-3-methylimidazolium bis(trifluoromethylsulfonyl)amide ionic liquids in an extended temperature range. *Fluid Ph. Equilibria* **2011**, *301*, 22–32, DOI: `10.1016/j.fluid.2010.10.018`.

75. Harris, K. R.; Woolf, L. A.; Kanakubo, M.; Rüther, T. Transport Properties of N-Butyl-N-methylpyrrolidinium Bis(trifluoromethylsulfonyl)amide. *J. Chem. Eng. Data* **2011**, *56*, 4672–4685, DOI: `10.1021/je2006049`.

76. Harris, K. R.; Kanakubo, M. Self-Diffusion Coefficients and Related Transport Properties for a Number of Fragile Ionic Liquids. *J. Chem. Eng. Data* **2016**, *61*, 2399–2411, DOI: `10.1021/acs.jced.6b00021`.

77. Kimura, Y.; Kida, Y.; Matsushita, Y.; Yasaka, Y.; Ueno, M.; Takahashi, K. Universality of Viscosity Dependence of Translational Diffusion Coefficients of Carbon Monoxide, Diphenylacetylene, and Diphenylcyclopropenone in Ionic Liquids under Various Conditions. *J. Phys. Chem. B* **2015**, *119*, 8096–8103, DOI: `10.1021/acs.jpcb.5b02898`.